Supplementary Information (SI) for Nanoscale.
This journal is © The Royal Society of Chemistry 2026

Supplementary Information

Kinetic-Dimension-Enabled Hydrogen Sensing via Spillover in Oriented Conductive Polymer Fiber Networks

Shiteng Wu[1], Mingyang Lu[1], Zerui Li[2,*], Yongbiao Wan[3], Fan Lei[4], Qi Yang[1], Kai Zhou[2], Guangxian Li[1], and Junlong Yang[1,*]

[1]College of Polymer Science and Engineering, State Key Laboratory of Advanced Polymer Materials, Sichuan University, Chengdu, Sichuan, 610065 China

[2]College of Electrical Engineering, Sichuan University, Chengdu, Sichuan, 610065 China

[3]Microsystem & Terahertz Research Center, Institute of Electronic Engineering, China Academy of Engineering Physics, Chengdu, 610200 China

[4]School of Mechanical Engineering, Chengdu University, Chengdu, 610106, Sichuan, China

*Corresponding authors: Zerui Li (lizerui@scu.edu.cn) and Junlong Yang (Email: yangjl@scu.edu.cn)

Supplementary Note S1 | Kinetic framework for concentration modulation and catalytic activity modulation caused by changes in adsorption sites:

For single-component hydrogen adsorption, the process follows classic Langmuir adsorption kinetics [1] :

$$\frac{d\theta_H}{dt} = k_a C_H(1-\theta_H) - k_d\theta_H \tag{S1}$$

Here, the θ_H represents the surface coverage of hydrogen, k_a and k_d denote the adsorption and desorption rates, respectively, and C_H is the hydrogen concentration. The solution of the equation is given as follows:

$$\theta_H(t) = \theta_\infty\left(1 - e^{-(t-t_0)/\tau}\right) \tag{S2}$$

$$\theta_\infty = \frac{K_H C_H}{1 + K_H C_H} \tag{S3}$$

This indicates that gas adsorption follows an exponential behavior, where $\theta_H(t)$ and θ_∞ represent the hydrogen surface coverage at time *t* and at saturation, respectively, and τ is the kinetic time constant. Accordingly, τ can be expressed as:

$$\tau = \frac{1}{k_a C_H + k_d} \tag{S4}$$

Therefore, for the response to single-component hydrogen. Under fixed experimental conditions, τ shows a significant negative correlation with the hydrogen concentration, and exhibiting a concentration-modulated behavior, and consistent with our experimental results.

On the other hand, for a fixed hydrogen gas concentration and a changed adsorption site. In general, noble-metal-modified sensors involve two processes, direct adsorption and a slower diffusion -mediated spillover. Since CO occupies H_2 adsorption sites under these conditions, the diffusion process must be considered, and the dual-channel response can be expressed as:

$$\Gamma(t) = \phi_0\left(1 - e^{-(t-t_0)/\tau_1}\right) + (1-\phi_0)\left(1 - e^{-(t-t_0)/\tau_2}\right), \quad 0 \le \phi_0 \le 1 \tag{S5}$$

where ϕ_0 is the weight of the direct adsorption, when CO randomly competes for H_2 adsorption sites, we set that it is a constant. And $(1-\phi_0)$ that of the slow diffusion-mediated pathway, $\tau_1$and τ_2 are their time constants, respectively. For comparison with concentration modulated behavior, we adopt a first order single exponential approximation：

$$\Gamma_{1st}(t) = 1 - e^{-\frac{t-t_0}{\tau_{eff}}} = \frac{t}{\tau_{eff}} - \frac{t^2}{2\tau_{eff}^2} + o(t^3) \tag{S6}$$

Where τ_{eff} is effective time constant, this approximation is obtained by matching the initial slope via a Taylor expansion [2], as detailed below：

$$\Gamma(t) = \phi_0\left(1 - \left[1 - \frac{t}{\tau_1} + \frac{t^2}{2\tau_1^2} - \ldots\right]\right) + (1-\phi_0)\left(1 - \left[1 - \frac{t}{\tau_2} + \frac{t^2}{2\tau_2^2} - \ldots\right]\right)$$

$$= \left(\frac{\phi_0}{\bar{\tau}_1} + \frac{1-\phi_0}{\tau_2}\right)t - \frac{1}{2}\left(\frac{\phi_0}{\tau_1^2} + \frac{1-\phi_0}{\tau_2^2}\right)t^2 + o(t^3) \tag{S7}$$

Hence, at $t \to t_0$ gives the closed form:

$$\frac{1}{\tau_{eff}} = \frac{\phi_0}{\tau_1} + \frac{1-\phi_0}{\tau_2} \tag{S8}$$

With the hydrogen concentration fixed, τ_1 remains approximately constant, and the saturation rate is then primarily determined by gas molecule diffusion and migration. The time constant can be estimated as:

$$\tau_{eff} \approx \tau_2 \approx \frac{L_{eff}}{D_{eff}} \tag{S9}$$

Where L_{eff} is the effective diffusion length and D_{eff} is the diffusion coefficient (the prefactor depends on boundary conditions). As gas molecules diffuse on the material surface, a reduction in adsorption

sites (in the presence of CO) can suppress trapping/polarization drag during migration [3], leading to an increase in D_{eff}, thereby reducing τ_{eff}. Consequently, hydrogen reaches a lower steady-state amplitude more quickly, which matches our observations.

To avoid the artifact that a smaller steady-state amplitude may look "faster or slower", responses are normalized to each condition's own steady (Figure **S**14). The trend of the saturation rate change and amplitude is consistent with this simplified model.

Table S1 | Performance comparison of reported PEDOT:PSS-based and representative metal oxide-based H_2 sensors.

Materials	**Structure**	**Method**	**Temperature**	**LOD**	**Flexible**	**Estimate CO content**	**Ref.**
PEDOT:PSS /PEO@Pt	Highly oriented fiber film	Microadhesion spinning	RT	75 ppb	Yes	Yes	**This work**
Graphene/ PEDOT:PSS	Thin film	Drop casting	373 K	30 ppm	Yes	No	22
PEDOT:PSS@Pd	Gel fiber	Sol-gel process	RT	2500 ppm	Yes	No	21
Graphene/ PEDOT:PSS-PEO	Suspended fiber	Electrospinning	373 K	1 ppm	No	No	20
Pd-$W_{18}O_{49}$ Nanowire	Nanowire	Hydrothermal reaction	398 K	51 ppb	No	No	37
Pt-coated WO_3	Cross-stacked nanorods	Thermal evaporation	303 K	10 ppm	No	No	38
Ag-modified Tb-doped In_2O_3	Nanocomposite	Hydrothermal reaction	433 K	100 ppb	No	No	39
Pd-SnO_2/rGO	Nanocomposite	Hydrothermal reaction	633 K	500 ppb	No	No	40
Pd-Doped α-Fe_2O_3	Nanotubes	Electrospinning	673 K	50 ppb	No	No	41

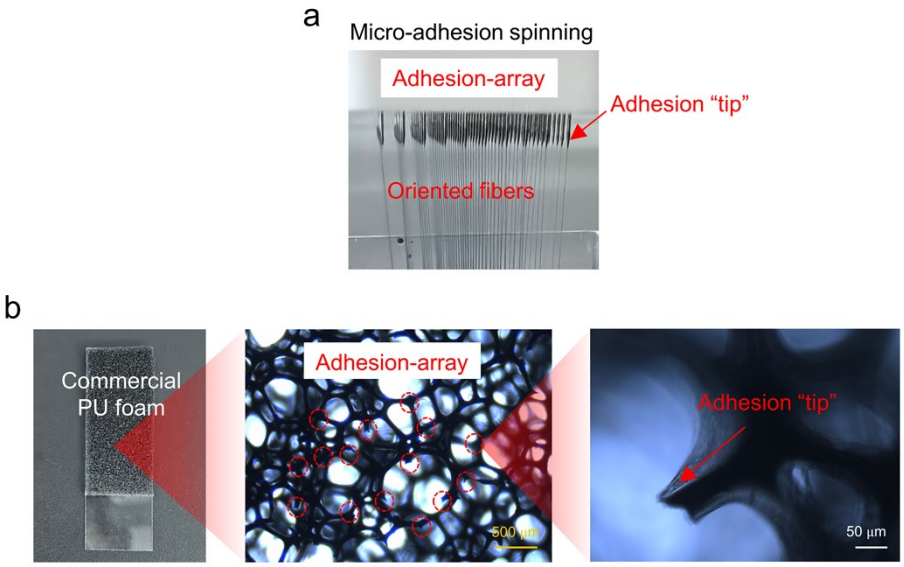

Figure S1 | (a) Photograph of the micro-adhesion spinning process. (b) Optical image of the PU foam used as the adhesion array for micro-adhesion spinning, showing the adhesion "tip".

Micro-adhesion spinning mainly relies on the microscale adhesion between the spinning solution and adhesion "tips", by which the spinning solution can be stretched into continuous fibers during the drawing process. This method does not require a strong electric field or air flow, and enables the rapid fabrication of oriented fibers with controllable alignment (Figure S1a). Here, to improve the efficiency of microadhesion spinning, we used a commercial open-cell PU foam (Hangzhou Gongshu Meimei Electronic Commerce Co., Ltd., China) as the adhesion-array. The abundant protrusions on the skeleton of the PU foam can serve as adhesion "tips" (Figure S1b), enabling the successful drawing of highly oriented fibers.

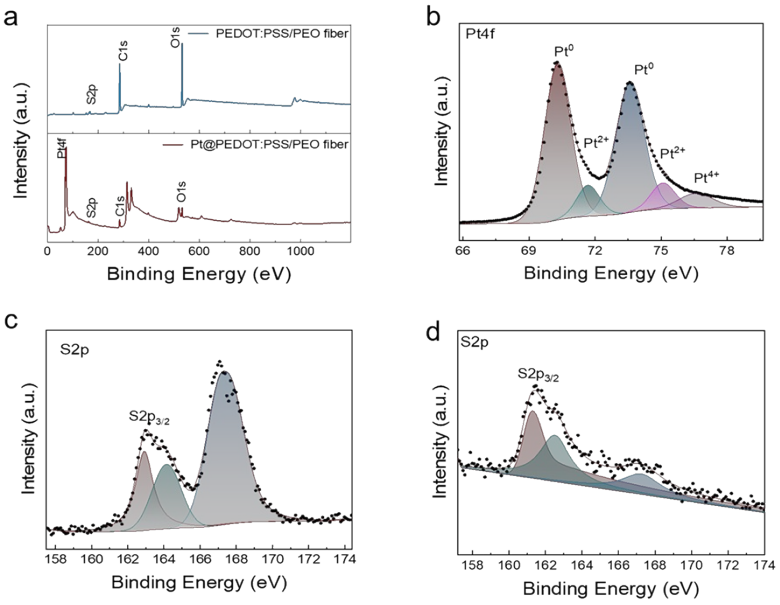

Figure S2 | XPS spectra of PEDOT:PSS/PEO and PEDOT:PSS/PEO @Pt. (a) Survey spectra. (b) Pt 4f spectrum. (c) S 2p spectrum of PEDOT:PSS/PEO. (d) S 2p spectrum of PEDOT:PSS/PEO @Pt.

The XPS survey spectrum (Figure S1a) of pristine PEDOT:PSS/PEO fibers shows C 1s, O 1s, and S 2p features. After Pt deposition (PEDOT:PSS/PEO@Pt), the S 2p intensity is markedly attenuated due to the Pt overlayer (short inelastic mean free path), and pronounced Pt 4f signals appear. The high-resolution Pt 4f spectrum (Figure S1b) was deconvoluted into two spin-orbit doublets, assigned to metallic Pt^0 (4f7/2 at 70.3 eV, 4f5/2 at 73.6 eV) and oxidized Pt^{2+} (4f7/2 at 71.7 eV, 4f5/2 at 75.1 eV); a weak shoulder at 76.6 eV is consistent with Pt^{4+} 4f5/2. Across the Pt 4f envelope, metallic Pt^0 is dominant, with a smaller fraction of oxidized Pt species. The S 2p spectra of PEDOT:PSS/PEO and PEDOT:PSS/PEO@Pt (Figures S1c,d) were fitted with thiophene-S (PEDOT) and sulfonate-S (PSS) components. After Pt loading, the main S 2p3/2 peak shifts by ~1.5 eV toward lower binding energy, suggesting that there may be an electronic interaction between PEDOT:PSS/PEO and Pt.

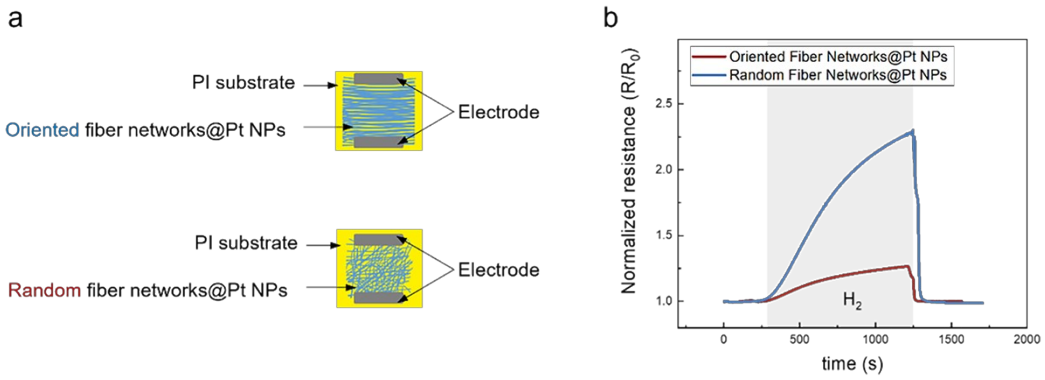

Figure S3 | Comparison of H_2 sensing performance between oriented and randomly oriented fiber networks.

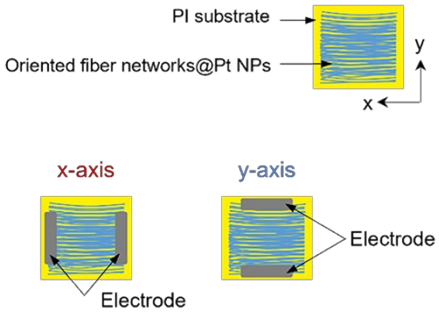

Figure S4 | The measurement and comparison methods of the resistance of the fiber network.

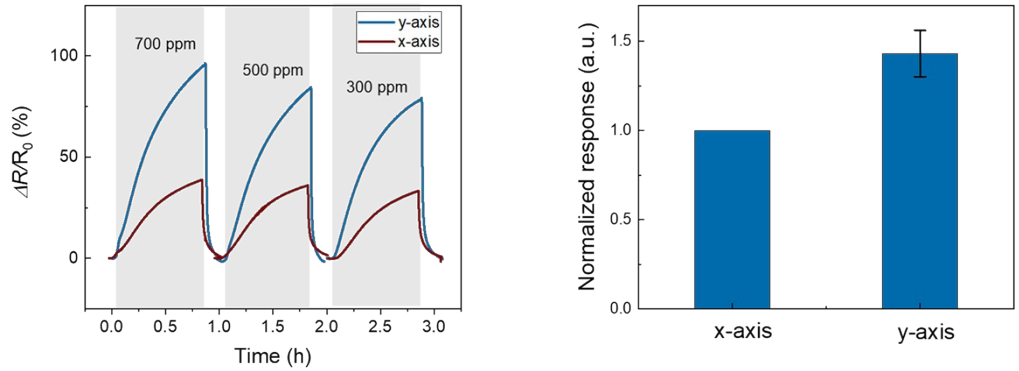

Figure S5 | Comparison of H_2 response characteristics of two charge transport paths for another sensor.

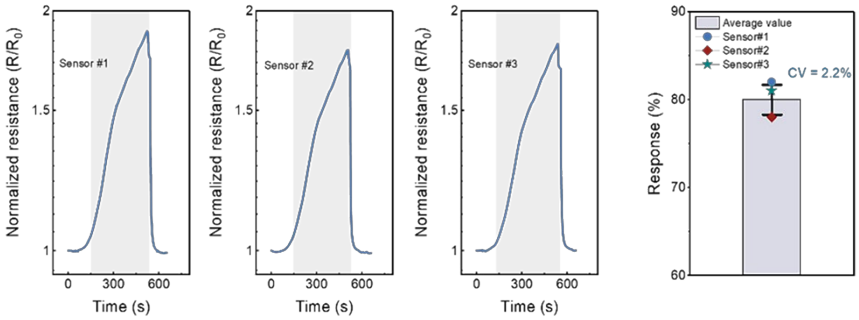

Figure S6 | H_2 responses of three different sensors prepared under the same micro-adhesion spinning conditions.

We compared the H_2 responses of three different sensors prepared under the same spinning cycles and spinning time, as shown in Figure S6. The three sensors exhibited similar responses, with a calculated coefficient of variation (CV) of only 2.2%. The CV was defined as $CV = (R_{SD}/R_{average}) \times 100\%$, where R_{SD} and $R_{average}$ represent the standard deviation and average response of the three sensors, respectively. This result demonstrates that controlling the drawing cycles and spinning time during the micro-adhesion spinning process can provide good reproducibility.

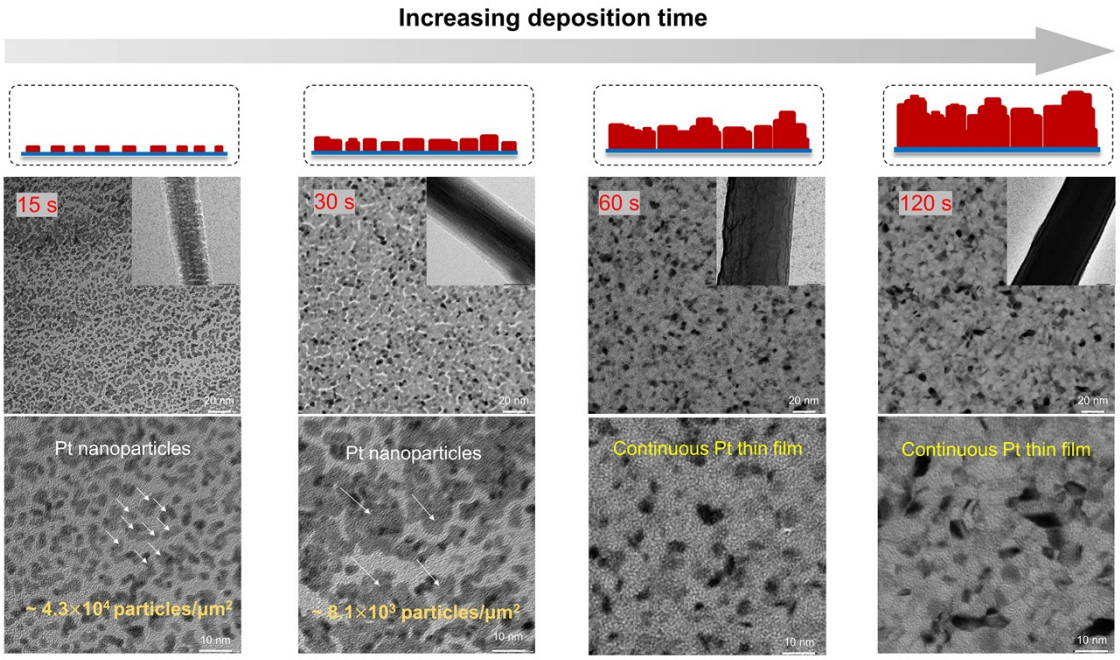

Figure S7 | Quantitative analysis of Pt nanoparticle density and TEM images of Pt nanoparticles under varying deposition times.

The optimal Pt nanoparticle density was 4.3×10^4 particles/μm^2 with an average particle size of 4 nm. The average inter-particle distance of 5 nm, implies the migration distance of the dissociated H on the PEDOT:PSS/PEO fibers. As the deposition time increases to 30 s, Pt nanoparticles merge and grow in size, indicating a reduction in nanoparticle density (~8.1×10^3 particles/μm^2) and an increase in their average size (~12 nm). As the deposition time further increases to 60 seconds and 120 seconds, the Pt nanoparticles interconnect to form a thin film. The optimal nanoparticle density (4.3×10^4 particles/μm^2) indicates that, on the one hand, smaller nanoparticle sizes offer a higher specific surface area, which provides more active sites to facilitate hydrogen dissociation, leading to shorter response time. On the other hand, it exposes more of the PEDOT:PSS/PEO surface, which aids in the modulation of the fiber's resistance by the dissociated H, thereby contributing to higher sensitivity and a lower detection limit.

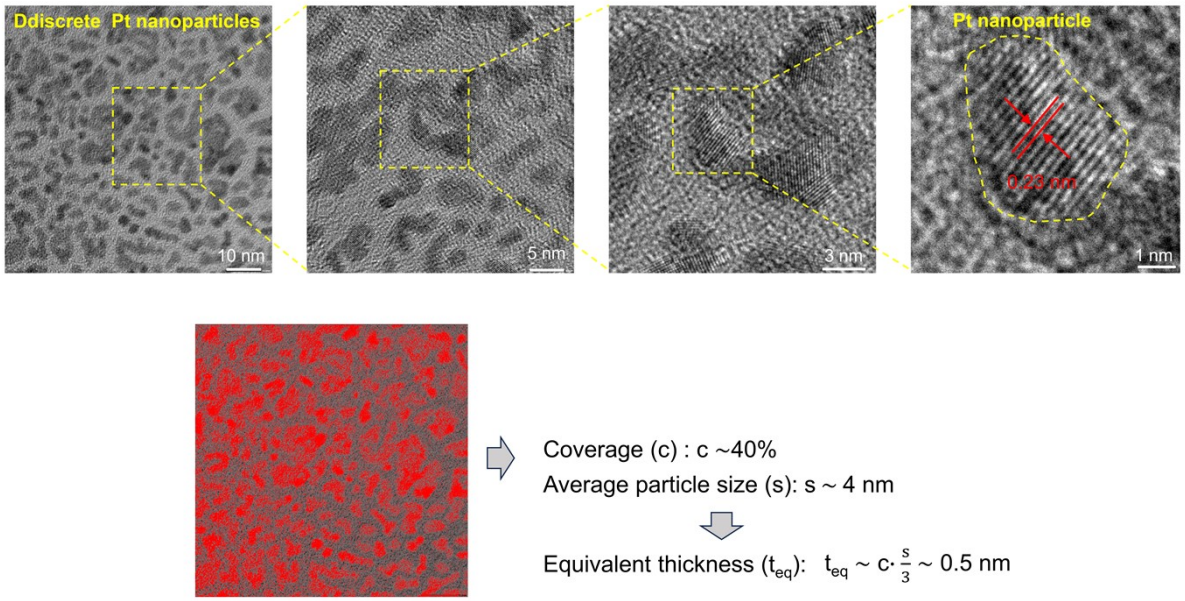

Figure S8 | Equivalent thickness estimation of the Pt-decorated layer based on the surface coverage and average size of discrete Pt nanoparticles.

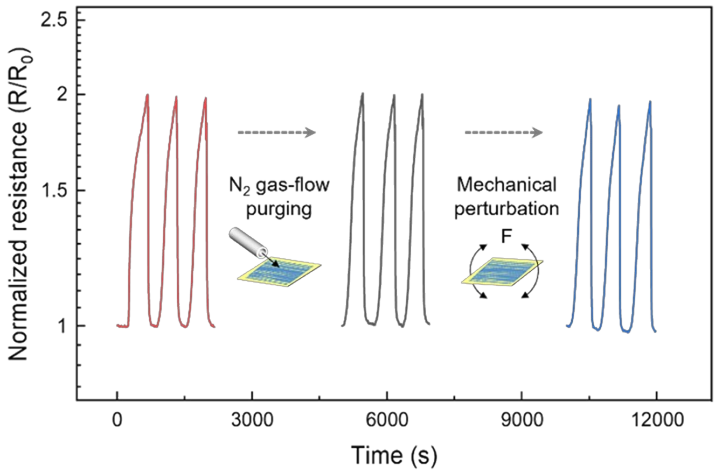

Figure S9 | Evaluation of the stability of Pt nanoparticles on the fiber network under N_2 gas-flow disturbance and mechanical bending.

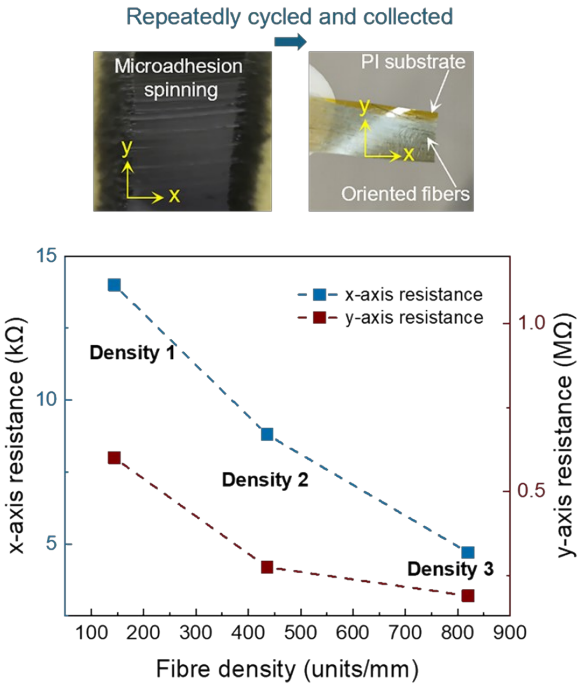

Figure S10 | Three fiber densities regulated by microadhesion spinning cycle time and their electrical properties in the x- and y-axis.

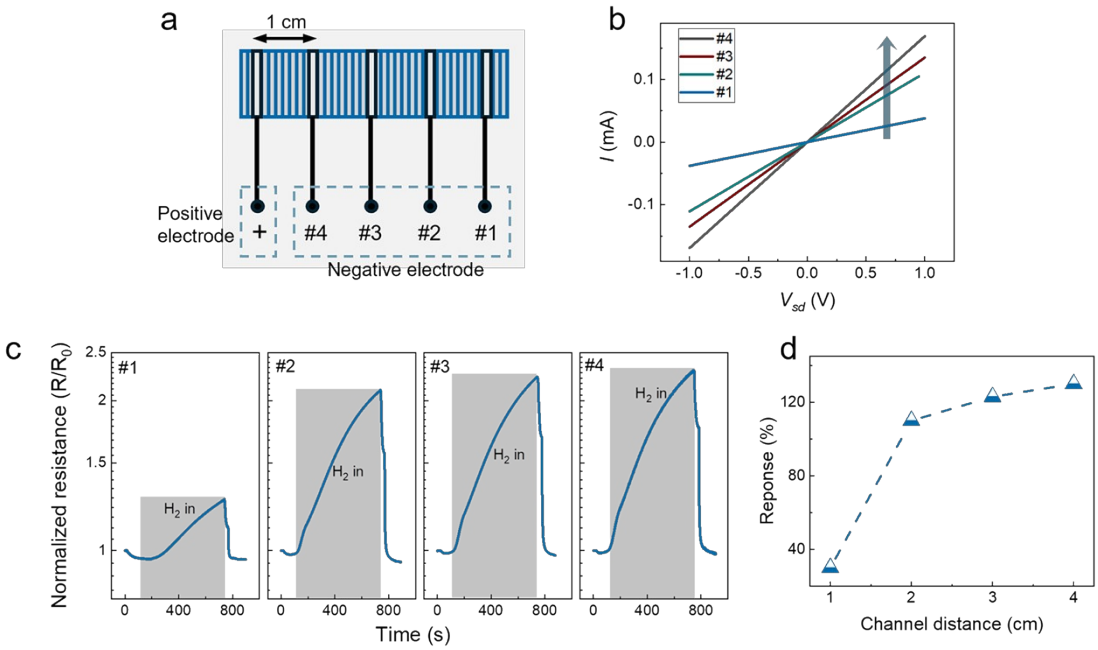

Figure S11 | Sensor size-dependent response characteristics. (a) Schematic diagram of the device with five electrodes and adjustable sensing channel length. (b) I-V curves for sensing channels with lengths of 1 cm, 2 cm, 3 cm, and 4 cm. (c) H_2 response characteristics of sensing channels with lengths of 1 cm, 2 cm, 3 cm, and 4 cm. (d) Comparison of R_s extracted from c.

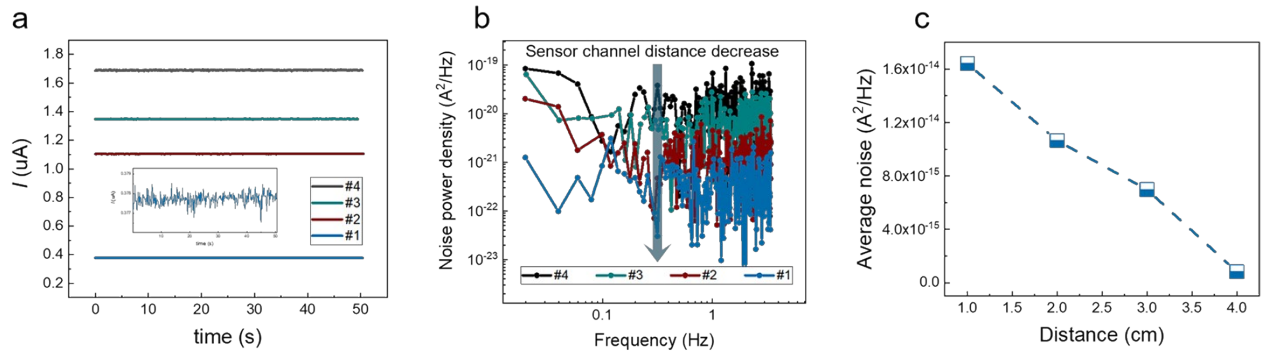

Figure S12 | Sensor size-dependent noise characteristics. (a) Current-time (I-T) curves for sensing channels with lengths of 1 cm, 2 cm, 3 cm, and 4 cm under a bias voltage of 0.01 V. (b) Noise power density of sensing channels with lengths of 1 cm, 2 cm, 3 cm, and 4 cm. (c) Comparison of the average of the noise power density extracted from b.

The device structure is shown in Figure S5a, with the device size of 1 × 4.5 cm and the distance between two neighboring electrodes ~1 cm, and four different sizes of 1×1, 1×2, 1×3, and 1×4 cm, and its I–V curves are shown in Fig S5b, which exhibit obvious resistance differences. Their response characteristics at 900 ppm H_2 concentration are shown in Figure S5c-d, where the responsivity increases instead as the device size decreases, which may be caused by the fact that longer device sizes have more defective states leading to trapping of the resistance during electron transport along the direction of the electric field, which results in a weakened contribution to the change in device resistance. The current-time (I-t) curves for four different sizes are shown in Figure S6a. Fluctuations of electrons during transport will lead to random ups and downs of the current signal (Figure S6a inset) i.e., generation of noise, which can be viewed as a superposition of sinusoidal signals of different frequencies. The noise spectral densities of four different device sizes can be obtained by Fourier transforming the I-t curves as shown in Figure S6b and comparing the average noise power of the device (Figure S6c), the results show that the noise signal decreases as the device size decreases, which may be caused by the electrons being subjected to fewer defective states being scattered along the shorter electron transport path.

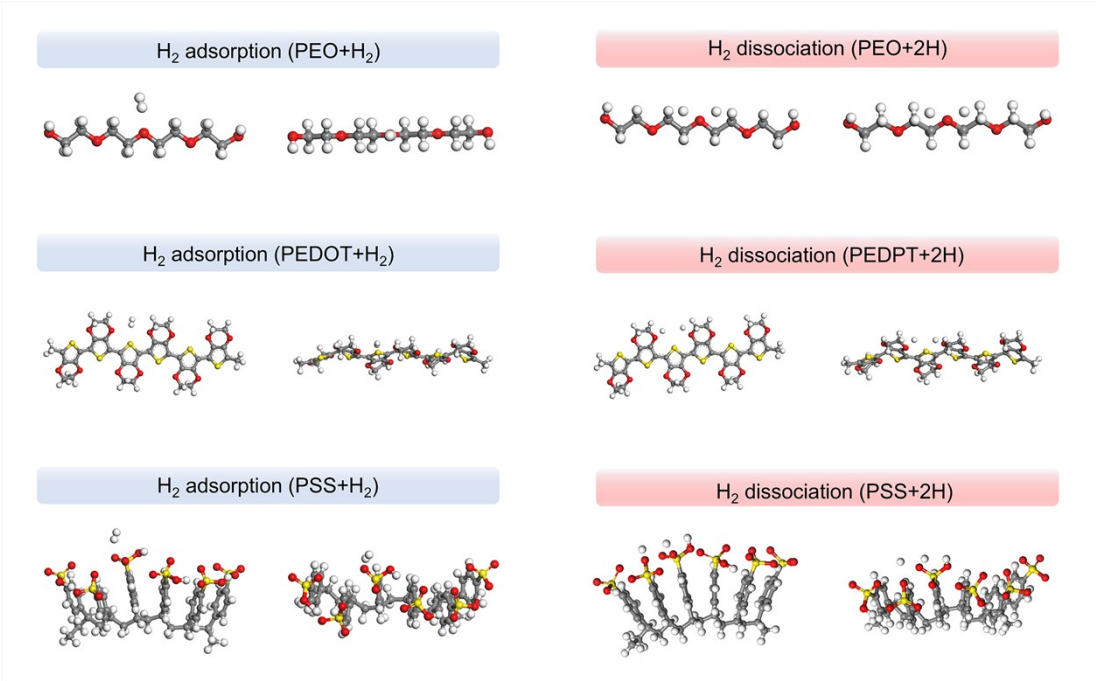

Figure S13 | Model clusters of the adsorption and dissociation of the H_2 molecules on PEO, PEDOT, and PSS.

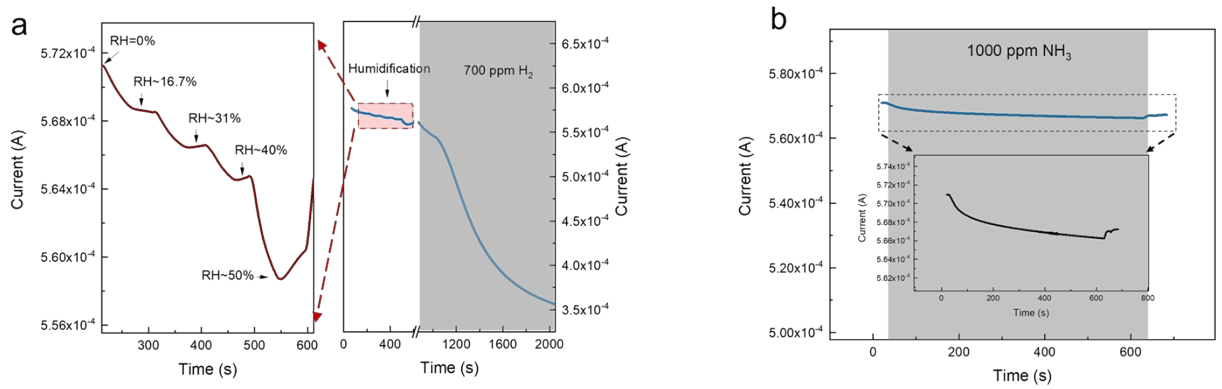

Figure S14 | The sensor's response to humidity and ammonia. (a) Humidity response adjusted via bubbling method. (b) Ammonia response measured by static testing method.

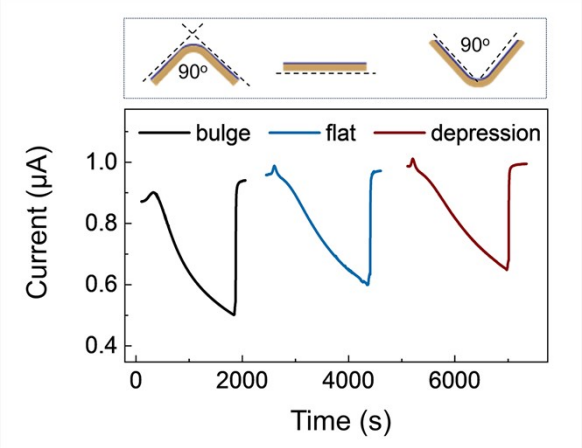

Figure S15 | Evaluation of the sensor performance under different mechanical conditions.

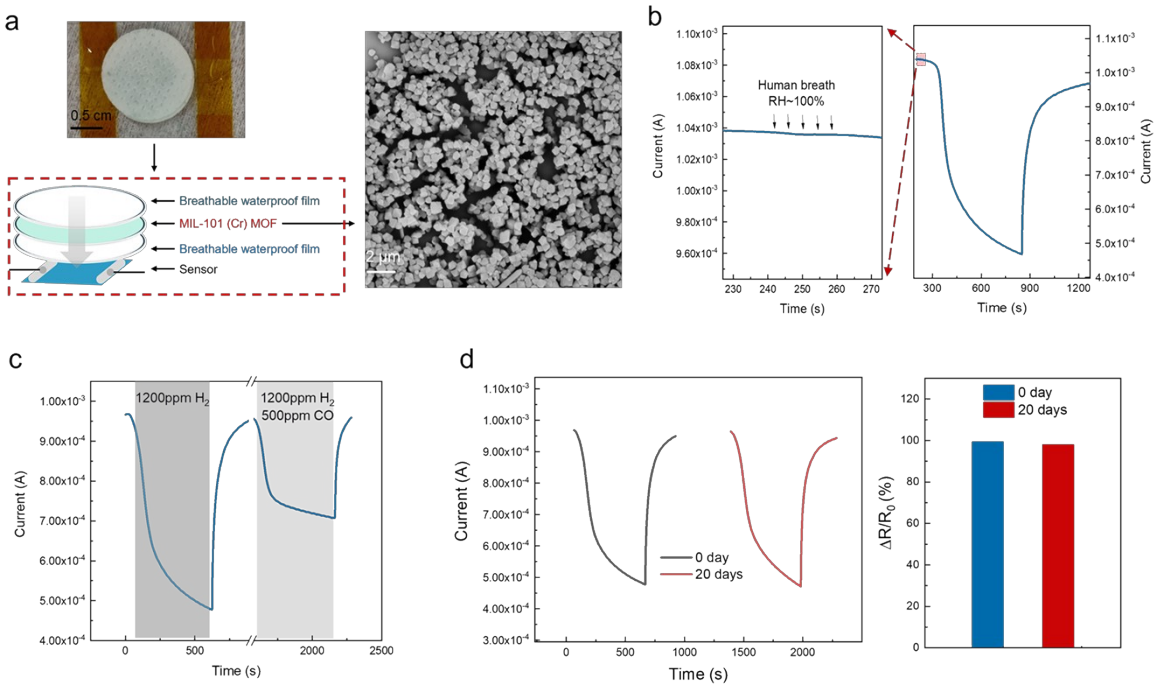

Figure S16 | Waterproof encapsulation of the sensor. (**a**) Schematic representation and photographic images of the encapsulation, along with the morphology of MIL-101 (Cr). (**b**) Sensor response to humidity after encapsulation, demonstrating its resistance to moisture-induced signal fluctuations. (**c**) Sensitivity of the encapsulated sensor to H_2 and CO, confirming maintained gas permeability. (**d**) Long-term stability of the encapsulated sensor, illustrating its sustained performance under extended operational conditions.

The encapsulation consists of two layers of breathable waterproof commercial PTFE membranes, with a layer of MIL-101(Cr) moisture-absorbing material inserted between them. This assembly is designed to effectively shield the sensor from moisture ingress while maintaining gas permeability.

The effectiveness of this encapsulation was validated under high-humidity conditions, such as exposure to exhaled human breath (RH ~100%). The results indicate that the sensor signal remained stable, with no significant fluctuations, while maintaining high sensitivity to H_2 (**Figure S8b**). Further validation showed that the encapsulated sensor remained permeable to H_2 and CO, as demonstrated in **Figure S8c**, while **Figure S8d** confirms that the encapsulation effectively preserves sensor performance over time. These findings highlight the robustness of our encapsulation strategy in ensuring sensor stability and reliability in humid environments.

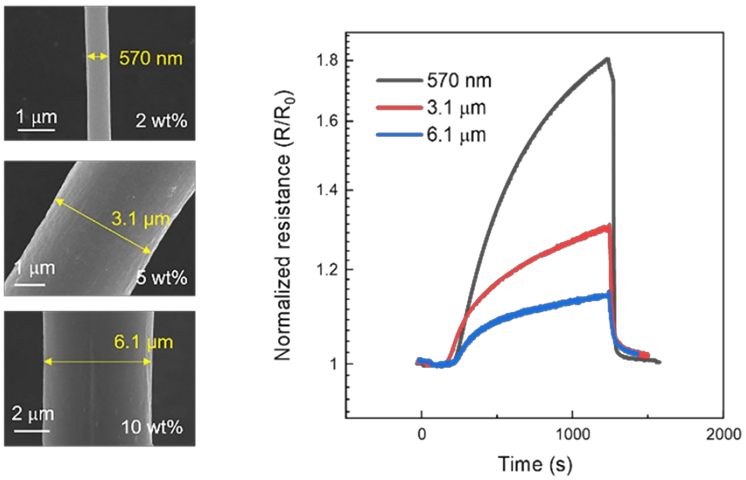

Figure S17 | Influence of fiber diameter on flexible H_2 sensing performance.

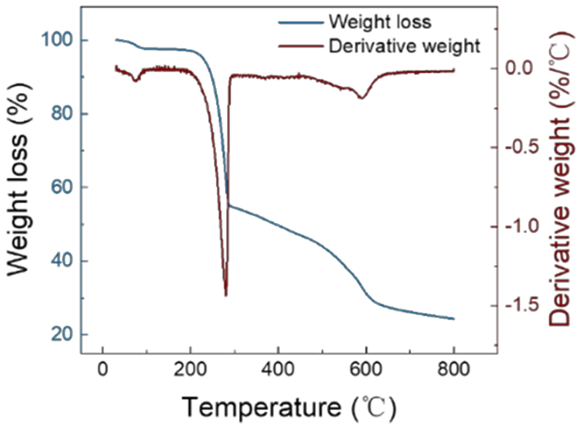

Figure R18 | Thermogravimetric analysis (TGA) curve of PEDOT:PSS/PEO under a nitrogen atmosphere with a heating rate of 10°C per minute.

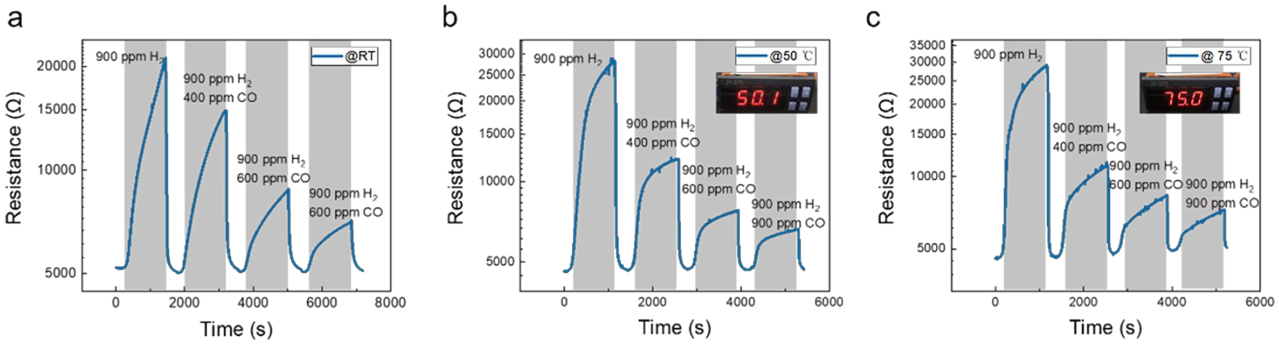

Figure S19 | Sensor response characteristics at room temperature, 50 ℃ and 75 ℃.

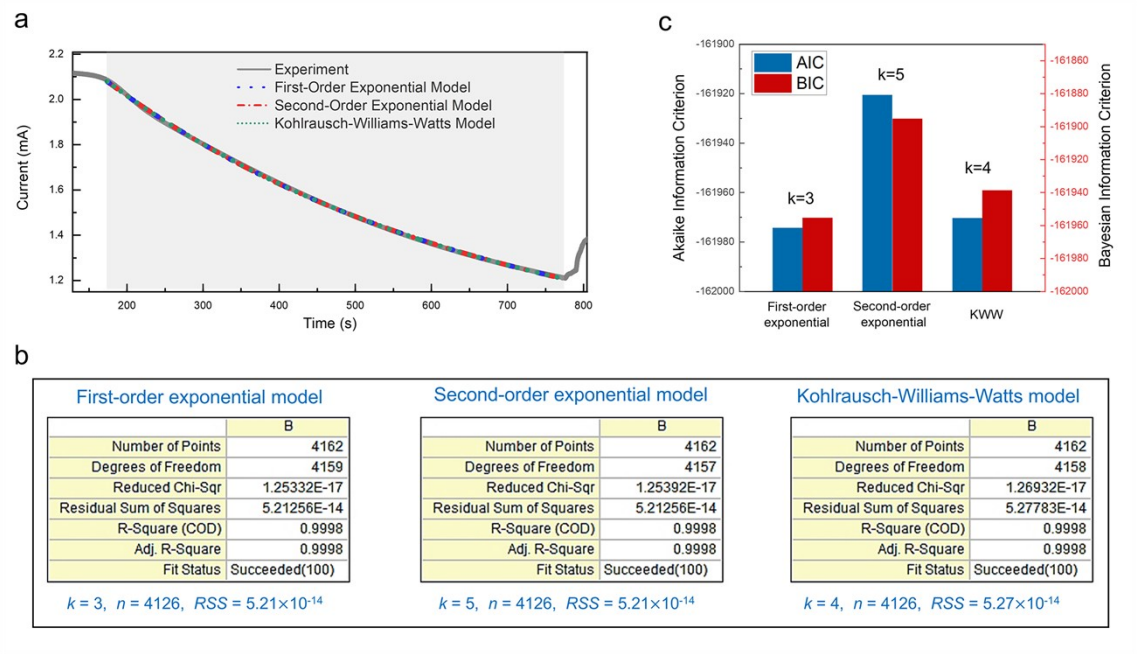

	B
Number of Points	4162
Degrees of Freedom	4159
Reduced Chi-Sqr	1.25332E-17
Residual Sum of Squares	5.21256E-14
R-Square (COD)	0.9998
Adj. R-Square	0.9998
Fit Status	Succeeded(100)

$k = 3,\ n = 4126,\ RSS = 5.21\times10^{-14}$

	B
Number of Points	4162
Degrees of Freedom	4157
Reduced Chi-Sqr	1.25392E-17
Residual Sum of Squares	5.21256E-14
R-Square (COD)	0.9998
Adj. R-Square	0.9998
Fit Status	Succeeded(100)

$k = 5,\ n = 4126,\ RSS = 5.21\times10^{-14}$

	B
Number of Points	4162
Degrees of Freedom	4158
Reduced Chi-Sqr	1.26932E-17
Residual Sum of Squares	5.27783E-14
R-Square (COD)	0.9998
Adj. R-Square	0.9998
Fit Status	Succeeded(100)

$k = 4,\ n = 4126,\ RSS = 5.27\times10^{-14}$

Figure S20 | (a) Response fitting with single-exponential, double-exponential, and KWW models. (b) Summary of fitting statistics, including degrees of freedom and residual sum of squares. (c) Comparison of AIC and BIC values, with smaller values indicating superior model performance.

We compared three standard exponential models on the same response curve—single exponential, bi-exponential, and stretched exponential (KWW) (Figure S11a). All three provided good fits. To prevent spurious improvements due to model complexity, we reported the residual sum of squares (RSS) together with two penalized model-selection criteria (AIC and BIC). When goodness-of-fit is comparable, smaller AIC/BIC values indicate a better balance between fit quality and parsimony. As shown in Figure S11c, both AIC and BIC attain their minima for the single-exponential model, indicating the most favorable trade-off under our experimental conditions. Although, in principle, the bi-exponential and KWW models could yield marginal RSS reductions, this was not observed here; even if such minor gains occurred, they would be offset by the penalty for reduced degrees of freedom, suggesting a risk of overfitting. Therefore, a single-exponential fit is sufficient to describe the response, and the extracted characteristic time τ is physically meaningful rather than a model artifact.

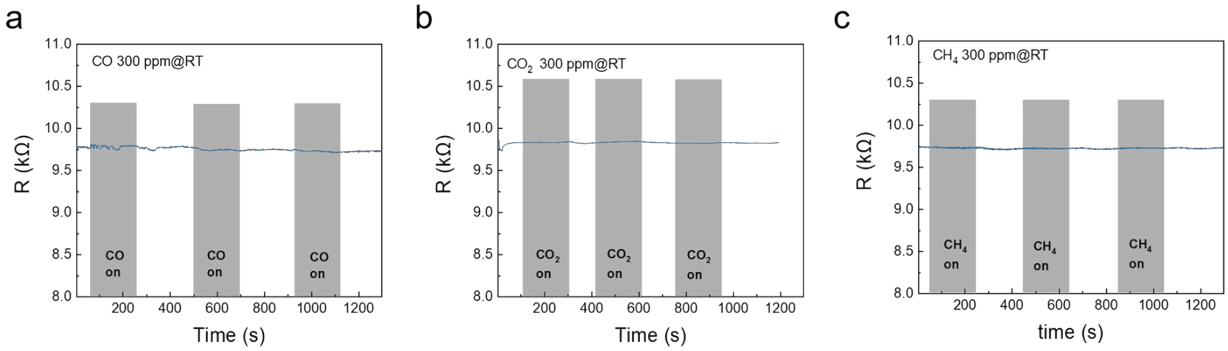

Figure S21 | Response characteristics of the sensor to (a) 300 ppm CO, (b) 300 ppm CO_2, and (c) 300 ppm CH_4 at room temperature.

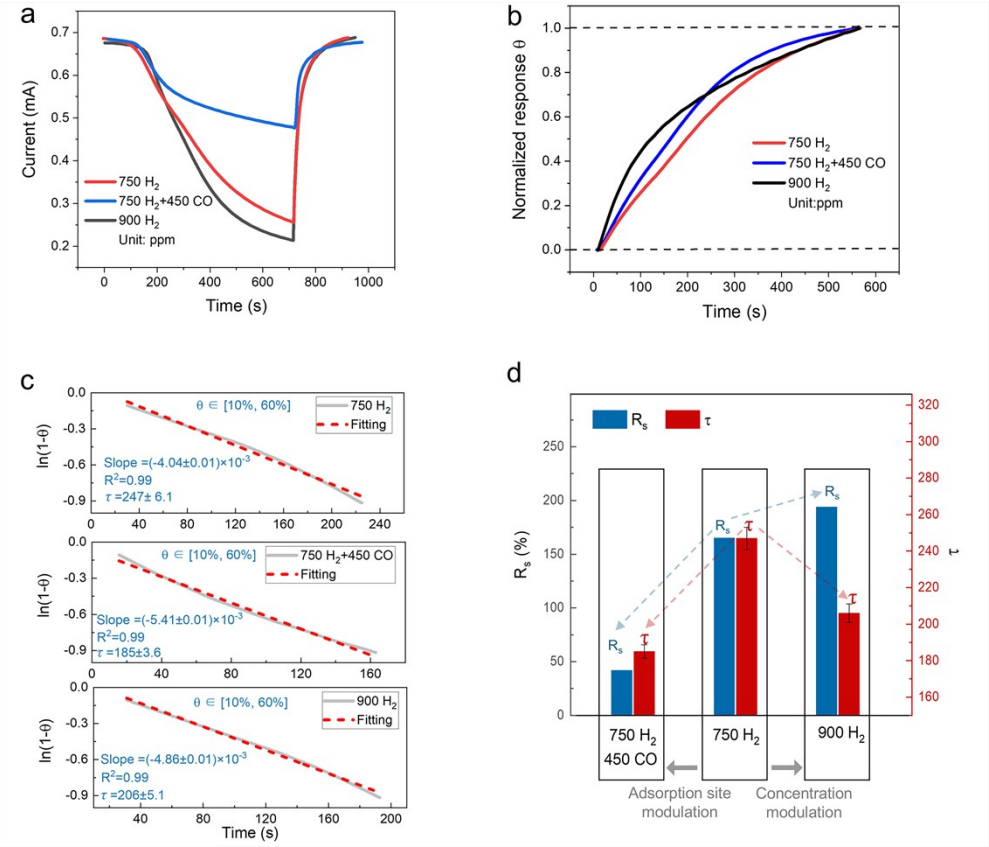

Figure S22 | Normalized kinetics and evidence for τ amplitude decoupling.

Response curves after normalization (Figures S13a and b), define $\theta(t)= (\Gamma(t)-\Gamma_0) / (\Gamma_\infty-\Gamma_0)$. Here, the Γ_0, $\Gamma(t)$ and Γ_∞ correspond to the signals at the initial moment, at time t, and at saturation, respectively. For single-exponential kinetics, $ln(1-\theta) = -t/\tau$. Thus, the $ln(1-\theta)$ vs. t slope depends only on τ and is completely independent of the response amplitude ($\Gamma_\infty-\Gamma_0$), any pure amplitude change is removed by the normalization and yields the same straight line with the same slope (Figure S13c). Therefore, when different conditions produce highly linear $ln(1-\theta)$ vs. t plots with stable slopes, τ is a kinetics-controlled time constant rather than a deformation parameter tied to amplitude. Conversely, if τ were amplitude-driven, one would expect curvature or systematic slope changes with amplitude, which are not observed. The extracted τ values and amplitudes under different conditions are shown in Figure S13d, exhibiting concentration-modulated and adsorption-site-modulated behaviors, respectively.

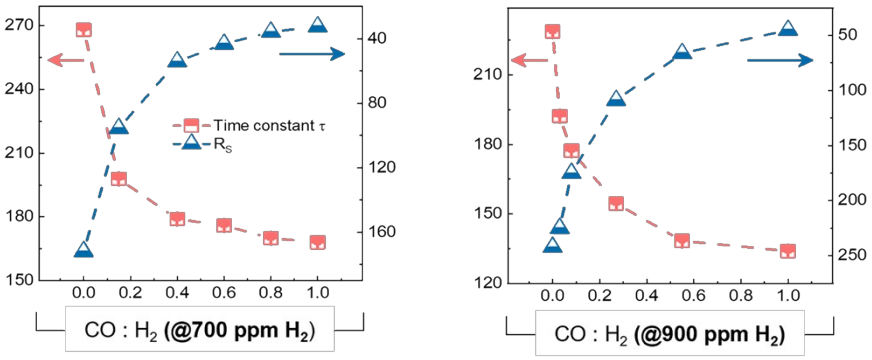

Figure S23 | R_s and τ under different concentrations and ratios of H_2 and CO gas mixtures.

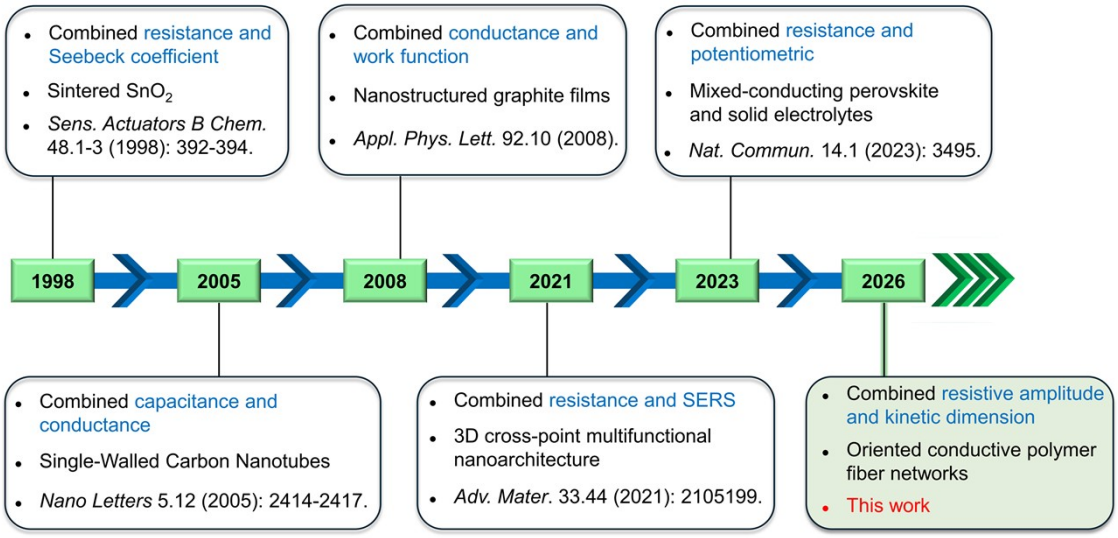

Figure S24 | Timeline chart showing the major developments in the expansion of output signal dimensions for chemiresistive gas sensors.

Supplementary references

1. Langmuir, Irving. "The adsorption of gases on plane surfaces of glass, mica and platinum." Journal of the American Chemical society 40.9 (1918): 1361-1403.
2. Mungan, Carl E. "Three important Taylor series for introductory physics." Latin-American Journal of Physics Education 3.3 (2009): 5.
3. Ala-Nissila, T., R. Ferrando, and S. C. Ying. "Collective and single particle diffusion on surfaces." Advances in Physics 51.3 (2002): 949-1078.